COBEM 2021 26th International Congress of Mechanical Engineering
November 22-26, 2021, Virtual Congress, Brazil

COB-2021-0767
Experimental Determination of the Parameters for the Rotary Friction Welding Process of Nickel Aluminum Bronze CuAl10Ni5Fe5

Daniel Pezza Tchernov
Francisco Yastami Nakamoto
Federal Institute of Education, Science and Technology of São Paulo - 625, Pedro Vicente Street, Canindé, São Paulo, SP, Brazil
tchernov.daniel@ifsp.edu.br; nakamoto@ifsp.edu.br

Mauro Machado de Oliveira
Federal Institute of Education, Science and Technology of São Paulo - 625, Pedro Vicente Street, Canindé, São Paulo, SP, Brazil
mauro.mo@ifsp.edu.br

Gilmar Ferreira Batalha
University of São Paulo - 2231, Professor Mello Moraes Avenue, Cidade Universitária, São Paulo, SP, Brazil
gilmar.batalha@poli.usp.br

Givanildo Alves dos Santos
Federal Institute of Education, Science and Technology of São Paulo - 625, Pedro Vicente Street, Canindé, São Paulo, SP, Brazil
givanildo@ifsp.edu.br

Abstract. *This work presents the investigation of solid-state joining processes with Rotary Friction Welding (RFW) of Nickel Aluminum Bronze (CuAl10Ni5Fe5). In order to optimize the welding parameters of the similar joints, the solution was deduced by applying Design of Experiments (DOE) approach based on Factorial Experimental Design with two levels and five factors. Initially, the solid rod work piece under this investigation were welded considering the literature reference and then established the levels of each parameter. Sequentially, the two levels of DOE were conducted by solid state union varying the defined parameters. For the purpose of investigate the thermal history during the process, temperature data has been acquired through infrared thermography to be compared with the temperature distribution obtained from the transient thermal analysis made on Ansys Workbench software. Metallographic, tensile test and micro-hardness measurements were used to determine the mechanical properties of the welded joints and the correlation with the optimal values parameters of the FRW process. As a result, it was found that the mechanical properties during the RFW process are altered by increasing the hardness of the diffusion interface.*

Keywords: *Rotary Friction Welding, Nickel-Aluminum-Bronze, Factorial Experiment, Thermography, Finite Element Analysis*

1. INTRODUCTION

Regularly, the most varied industrial sectors, in the development of their products, apply permanent and non-permanent joining techniques of metallic and non-metallic parts. Among the various joint solutions available, friction welding processes have been gaining prominence since the process does not form a molten pool, solidification-related problems do not occur, and it is its principal benefit to mechanical applications. (Cai, *et al.*, 2019). In the work by Maalekian (2007), friction welding processes are classified according to the relative movements shown between the parts, which can be i) rotational friction welding ii) linear friction welding and iii) orbital friction welding. Given the above, Figure 1, proposed by Maalekian (2007) shows us the parameters to be controlled during the process, initially with the rotation speed, time and friction pressure (heat-up stage), time and forging pressure (burn-off and forging stage). One of the most important processes of solid-state joining is called Rotary Friction Welding (RFW) and and will be applied in this study. Its principle refers to a relative movement between two workpieces that works by rotating one against the other while a compressive axial force is applied, which produces coalescence of materials workpieces (Vairis, *et al.*, 2016). The process variables mentioned will be studied through the Fractional Factorial Experiment, representing their levels.

According to Richardson (2016), Nickel Bronze Aluminum (NAB) alloys are so classified when they contain between 6 to 13% aluminum, up to 7% iron and nickel, respectively. This material has applications in several segments depending on its properties, such as i) naval: manufacture of ship thrusters due to its high resistance to corrosion and marine biofouling ii) petrochemical: manufacture of actuating valves used in environments susceptible to explosion, since the material does not produce sparks iii) aeronautics: used in landing gear bearings and plane flaps due to its excellent

mechanical and wear resistance, low density and damping capacity iv) casting: pump and valve housings on account of its high resistance to cavitation.

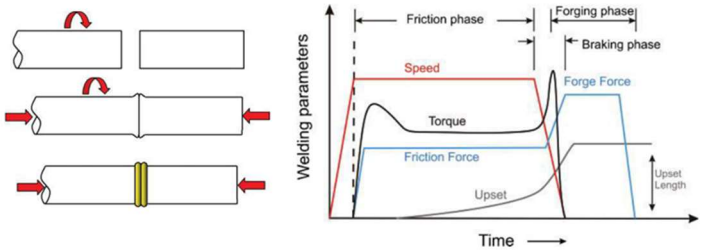

Figure 1. Diagram of the rotational friction welding process with the indication of the phases present.

Recent work has investigated NAB friction welding. For example, Küçükömeroğlu et al. (2016) successfully applied friction stir welding to alloy C95800 for their experiments varying the process parameters. Simultaneous recrystallization, grain refinement and excessive plastic deformation in the stir zone were observed, in addition to the appearance of the Widmanstätten morphology with the increase of the stir intensity of the material. There was an increase in hardness and all the produced joints exhibited values of tensile strength and fracture toughness similar or superior to the base metal. In this same sense, Selvaraju et al. (2018) and Siva et al. (2019) conducted their experiments reaching similar conclusions, that is, the occurrence of dynamic recrystallization, grain refinement, microstructural and mechanical properties changes. After these verifications, it was possible to observe that the NAB arouses interest on the part of researchers, more specifically with the application of friction stir welding, however, there was a lack of studies of this same material with the use of rotational friction welding, being one of the great motivations of this article.

2. METHODOLOGY

The methodology proposed for this work aims to reconcile experimental and numerical-computational procedures, thus, a literature search was carried out to satisfy this condition. According to Schwer (2006), there are a series of rules to be followed to run a computer simulation. The starting point is the identification of the problem, that is, which physical system to model. Subsequently, hypotheses and descriptions are defined, and a mathematical model is created, making it possible to carry out experimental procedures and later validate the results. Figure 2 shows the plan used to conduct this research.

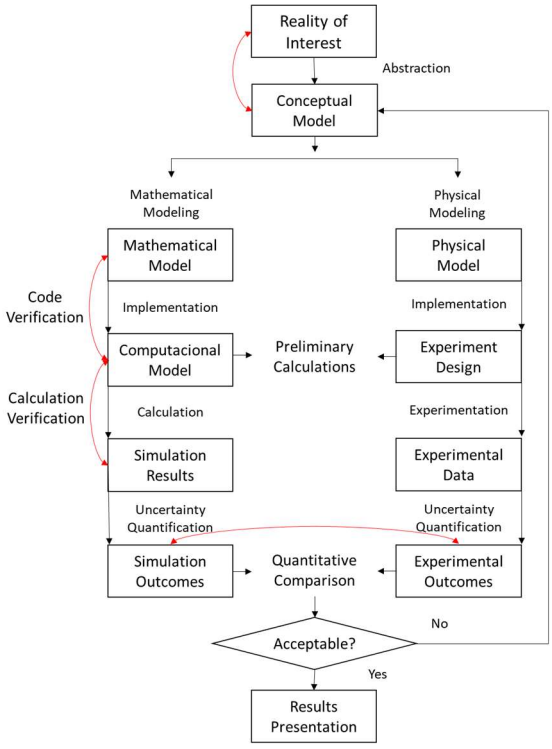

Figure 2. Schematic diagram of the search strategy.

2.1 Materials

The manufacturing process of samples of Bronze Aluminum Nickel CuAl10Ni5Fe5 (i.e., UNS 630) initially involved horizontal continuous casting and hot extrusion process, afterwards, its mechanical properties were improved with drawing and tempering. Thus, cylindrical bars with a diameter of 15.87 mm (± 0.08) according to the ASTM B249 standard and a grain size of 0.010 mm were used in this experiment. Its chemical composition can be seen in Table 1, where we can observe the values referenced by DIN 17665 and the chemical composition obtained by the manufacturing process described above designated by measured weight.

Table 1. Chemical composition of the NAB alloy used according to the DIN 17665 in comparison to the tested values.

Elements	Cu	Al	Ni	Fe	Mn	Pb	Others(1)
Nominal Weight (%)	remainder	8.5 to 11	4 to 6	2 to 5	1.5	0.05	-
Measured Weight (%)	80.74	10.76	4.53	3.67	0.074	0.011	0.127

(1) Others Si, Sn, Zr, Co, Pb, Mg, Be and Cr

The tensile tests were carried out in accordance with the standard ABNT NBR 6892-1: 2013 and their results can be seen in Table 2 where the nominal values and those obtained experimentally are referenced. Note that the mean values of the tensile strength limit, yield limit and total elongation are substantially higher.

Table 2. Typical mechanical properties of the NAB alloy used.

Properties	Tensile Strength (MPa)	Yield Strength (MPa)	Elongation (%)	Hardness Brinell
Nominal value	600.0	250.0	13.0	140.0
Measured value	809.6	655.0	30.0	255.0

The Fractional Factorial Experiment 2^{5-1} was carried out on two levels and one repetition. To define the factors and their levels, they were used as a reference for the copper factors extracted from the literature. The planning matrix was performed with the aid of the Minitab® 18.1 statistical software and the values of the welding parameters can be found in Table 3.

Table 3. Weld parameters used.

Specimen	Sequency	Speed (rpm)	Friction Pressure (MPa)	Friction Time (s)	Forge Pressure (MPa)	Forge Time (s)
1	1	3000	0.3	10	4	15
2	4	3300	0.5	10	4	15
3	8	3300	0.5	17	4	10
4	3	3300	0.5	10	4	10
5	10	3000	0.3	10	5	15
6	2	3300	0.3	10	4	10
7	6	3300	0.3	17	4	15
8	9	3300	0.3	10	5	10
9	13	3000	0.3	17	5	15
10	11	3000	0.5	10	5	15
11	15	3000	0.5	17	5	10
12	16	3000	0.5	17	5	15
13	7	3300	0.5	17	4	15
14	12	3000	0.5	10	5	10
15	14	3300	0.3	17	5	10
16	5	3300	0.3	17	4	10

The workpieces were cutted and faceted to a length of 65 ± 0.3 mm and divided into three different batches. The first and second batches were reserved to weld the joints with the parameters indicated in Table 3 and the third to weld the joints with the optimal parameters found by the method of the factorial experiment. The process capacity indices were calculated for the lengths and can be consulted in Table 4. The average surface roughness (Ra) of one of the faces was analyzed with a portable roughness meter, accuracy of ± 10%, cut-off of 0.8 mm and evaluation length of five times, having been considered a roughness class of 0.8 μm (N6).

Table 4. Process capacity indices for the length of the workpieces.

Batch	σ_0 (mm)	C_p	C_{pk}
1	0.075	1.33	1.25
2	0.092	1.09	0.92
3	0.062	1.61	1.49

The instrumentation of the welding process took place using a FLIR28 model T400 thermographic camera. The equipment was positioned with the use of a tripod in a non-perpendicular way, 0.7 meters away from the workpieces, as shown in Figure 3, the emissivity was set to 0.84 at an ambient temperature of 22.9°C, relative humidity of 70% and temperature reading range of 200 to 1200°C and accuracy of 2% when making measurements. The images were captured at the end of the warm-up phase, at 7 seconds and 14 seconds, respectively, for a warm-up time of 10 and 17 seconds.

Figure 3. Scheme of the rotary welding machine and the thermography camera.

2.2 Finite Element Analysis Modeling

For the finite element numerical simulation, a 3D non-linear axisymmetric thermal model was created with the Transient Thermal module of the Ansys Workbench 19.2 software in order to find the temperature gradient along the longitudinal axis. Figure 4 shows the model geometry, connections, mesh, boundary conditions and loads. The mesh was made up of tetrahedral elements of size 3.5 mm with refinement in the diffusion interface, adding 16,245 knots and 10,477 elements. The contact used was of the friction type with a coefficient of 0.3. The temperature of 552.0°C found by the thermography was inserted in the diffusion interface, as well as the effects of convection and radiation. The specific gravity of the material is 7.5 g / cm³ (at 20°C), thermal conductivity of 37.7 W / m.K and heat transfer coefficient adopted of 25 W / m².K.

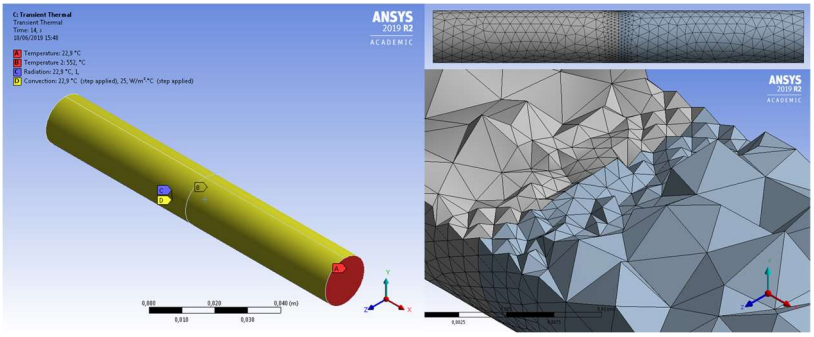

Figure 4. Boundary conditions and loadings applied to the model by finite elements (left) and mesh refinement detail (right).

The mathematical models that describe the rotational friction welding process in terms of heat generation and thermal transfer will be presented below (Thien, *et al.*, 2016).

$$q = \frac{\mu\pi^2 R^3}{45}.P_1.n \quad (1)$$

Where: **q**, **R**, **P1** and **n** are the heat needed to join the work pieces, workpiece radius, friction pressure and rotation, respectively.

$$T(x) = T\infty + \frac{q_s}{\sqrt{hpkA}} \frac{\cosh[m(L-x)]}{\cosh(mL)} \quad (2)$$

Where: **T**, **T∞**, **h**, **p**, **k**, **A**, **m** and **L** are the temperature at position x, room temperature, heat transfer coeficiente, workpiece circumference, thermal conductivity, workpiece cross-sectional área, x-axis variable and workpiece length, respectively.

3. RESULTS AND DISCUSSION

The joints were welded according to the parameters in Table 1. During the tests, images were taken with the aid of a thermographic camera (see Figure 5) and, subsequently, with the joints at room temperature, their lengths were measured with a caliper. 0.002 mm resolution for determining axial reduction. This information is recorded in Table 1, where it is possible to observe that there was variation between the tests performed for the first and second batches, considering the same welding parameters. This difference can be explained by the uncertainties of the equipment, with, for example, its rigidity and control system, since it is a conventional lathe that was originally adapted to a conventional friction welding machine. Figure 1 illustrates the metal joints obtained by the process described above, where it is possible to verify the formation of the characteristic burr, and Figure 1 reveals the temperature gradient by means of thermography in the welding region.

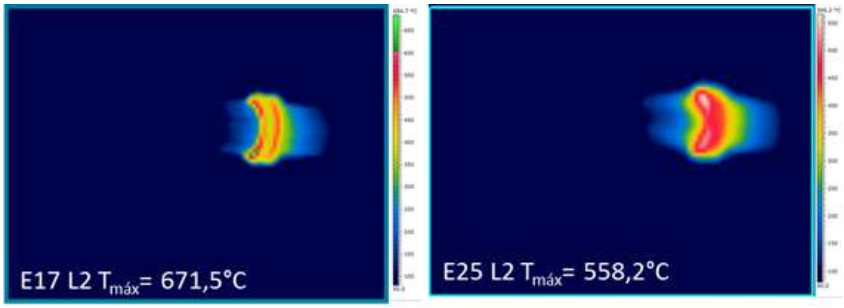

Figure 5. Thermographic images taken during the rotational friction welding process.

Table 5. Weld parameters used.

Specimen 1st Batch	Axial Shortening (mm)	Temperature (°C)	Specimen 2nd Batch	Axial Shortening (mm)	Temperature (°C)
1	5.70	189.60	17	1.46	671.50
2	3.26	454.30	18	1.04	186.20
3	6.94	379.10	19	10.4	459.20
4	1.32	342.90	20	0.00	182.90
5	3.34	454.60	21	0.00	194.70
6	1.66	193.90	22	0.08	164.20
7	12.92	507.90	23	9.98	552.00
8	0.00	173.80	24	0.00	143.40
9	11.40	492.00	25	8.30	558.20
10	0.00	167.10	26	0.00	141.60
11	9.34	529.40	27	6.50	514.80
12	10.30	552.00	28	5.60	525.50
13	9.30	501.80	29	11.46	465.80
14	1.16	231.90	30	9.98	162.10
15	10.22	413.30	31	9.82	537.40
16	9.76	539.40	32	9.44	508.80

3.1 Finite Element Analysis Results

The finite element analysis aimed to investigate the thermal history through the temperature gradient and heat flux as shown in Figure 6, to validate the finite element model, the minimum temperature of the simulation was analyzed with the respective thermogram therefore, a percentage error of less than three was found. Furthermore, it can be observed that

the heat flow travels along the longitudinal direction of the workpieces, totaling approximately 20 mm from the diffusion interface for each body, that is, in this stretch of material, the microstructural changes are more likely to occur.

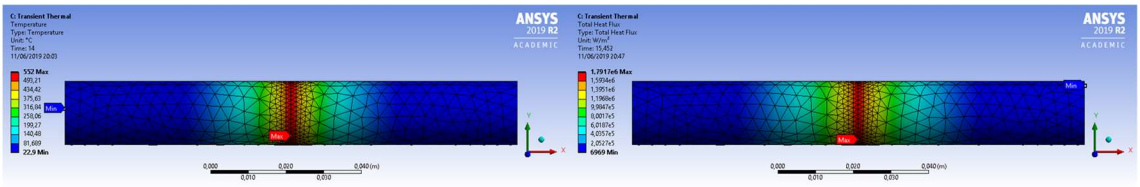

Figure 6. Transient thermal simulation for temperature gradient (left) and heat flux (right).

3.2 Tensile Properties of the Welded Joints

The tensile properties of the welded joints were extracted and can be found in Table 1. Given this information, we can make some comparisons with the tensile test conducted previously with material samples provided by the manufacturer. Therefore, the mean values of tensile strength, yield strength and total elongation were lower than the base metal as can be seen below.

Table 6. Tensile test results of the NAB alloy used.

Properties	Tensile Strength (MPa)	Yield Strength (MPa)	Elongation (%)
Before union	809.6	655.0	30.0
After union	664.0	417.6	7.6

Figure 7 (on the left) shows the stress-strain curve in which it is possible to observe that right after the material flows, there is little plastic deformation and the material already ruptures. The images on the right place the test specimens tested side by side in the receiving condition and after welding. Therefore, there is a ductile behavior before welding and a fragile behavior after welding, in which the rupture occurs in the welding region, an undesirable result for welded joints. This behavior can be induced by an increase in hardness in this region and will be discussed later.

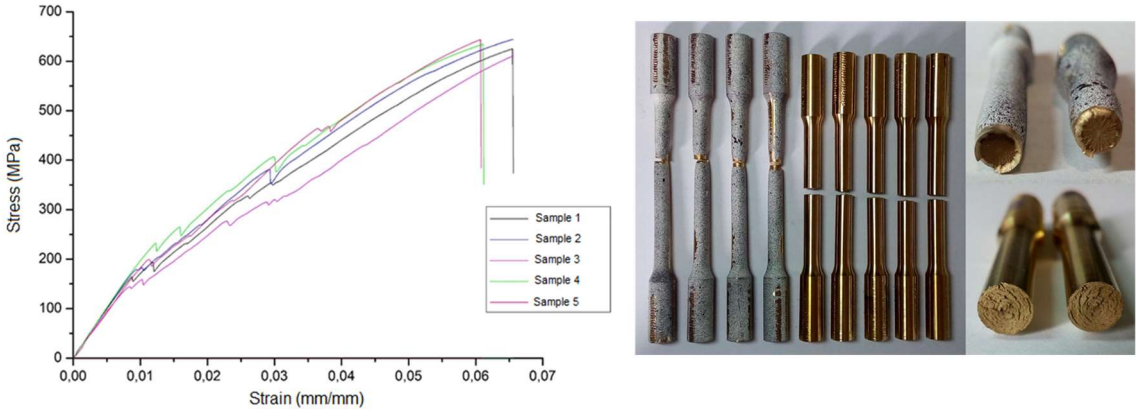

Figure 7. Stress-strain graph and tested specimens.

3.3 Microstructure

For this study, the preparation of samples for metallographic tests was established in accordance with the ASTM E3-95 standard. For this purpose, the longitudinal sections of three samples were cut from the welded parts as shown in Figure 8. The chemical attack was carried out in accordance with the ASTM E407-99 standard in a solution composed of 50 % HNO_3 (nitric acid) and 50 % water in a time of approximately 7 seconds for micrographic test samples.

Figure 8. Cutting scheme for obtaining samples for metallographic analysis and macrograph with 70X magnification.

Micrographic analyzes were conducted using an upright material microscope with universal LED illumination Leica Microsystems model DM2700 M equipped with a high-speed color EC3 digital camera and Leica Application Suite software (v4.12.). The first photomicrographs taken were grouped side by side, resulting in the image seen in Figure 9 in which the different regions of the body of evidence can be observed. The Weld Centre Zone (WCZ) comprises the diffusion interface and presents significant grain refining, adjacent to this, we have the Thermomechanically Affected Zone (TMAZ). Moving towards the ends, we check the Heat Affected Zone (HAZ) with the visible effect of the material mixture and, finally, the Base Metal with the original characteristics of the material, that is, before the welding process.

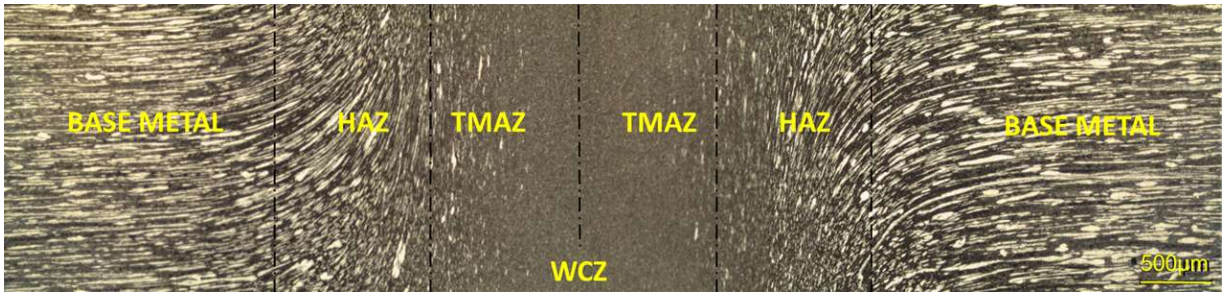

Figure 9. Photo sequence of the assay with 50X magnification and 500 µm linear size scale.

The most significant microstructural changes occurred in the central welding zone with decreasing grain size. Composed of an intermediate structure and a predominance of Alpha (α) phase with Widmanstätten morphology and Beta (β) phase retained, created above the eutetoid point of the material, thus forming a martensitic structure with high densities of NiAl precipitates, very fine and identified by darker areas. In Figure 10 below, it is possible to see the first intermetallic formed in the solidification phase, called $Kappa_I$, it has a rosette shape and is rich in iron. Below 930°C we have the formation of spheroidalized intermetallic $Kappa_{II}$ distributed at the (α)/(β) interface. Subsequently at 860°C, when the solubility of iron is exceeded, fine $Kappa_{IV}$ intermetallic forms within the grains. Finally, at 800°C the Beta (β) phase not yet transformed generates the intermetallic $Kappa_{IV}$ in the eutetoid reaction $\beta \rightarrow \alpha + K_{III}$ presenting a lamellar shape in the grain boundary.

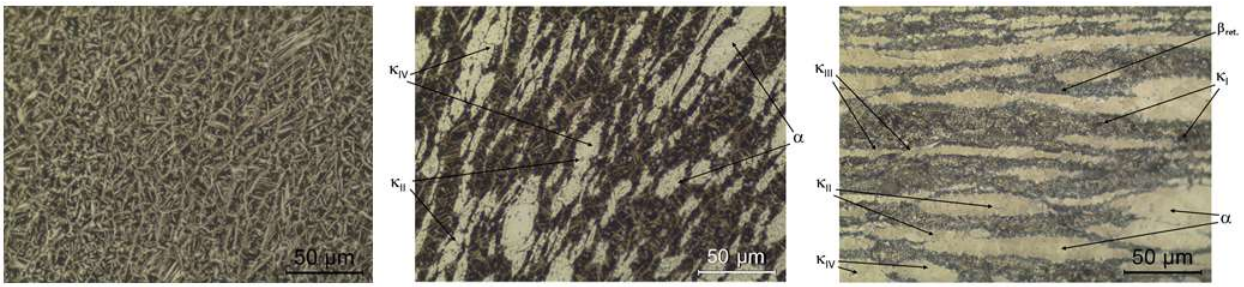

Figure 10. Micrograph: WCZ showing Widmanstätten (left), TMAZ (center) and HAZ (right) with 500X magnification.

3.4 Microhardness

The Vickers HV 1 microhardness test was carried out in accordance with the ABNT NBR NM 6507-1:2008 standard using the Vickers Future Tech FM 110 digital microhardness meter. The applied load was 9.8 N for a time of 15 seconds

at temperature ambient 22°C. The indentations covered the total length of 22 mm in the longitudinal direction of the sample at three different levels – separated by 5 mm between them – above, in the center and below, varying from 1 mm to each level. The adopted scheme can be better visualized in Figure 11, as well as the results obtained. It is possible to observe at coordinate zero (equivalent to WCZ) a significant variation between measurements, with 420.5 HV 1 (above), 273 HV 1 (in the center) and 323.7 HV 1 (below) against 258.1 HV 0 ,1 measured before the solid-state welding process. This increase in Hardness can be explained by the presence of the Beta phase (β) retained in the WCZ verified in the micrographs seen above.

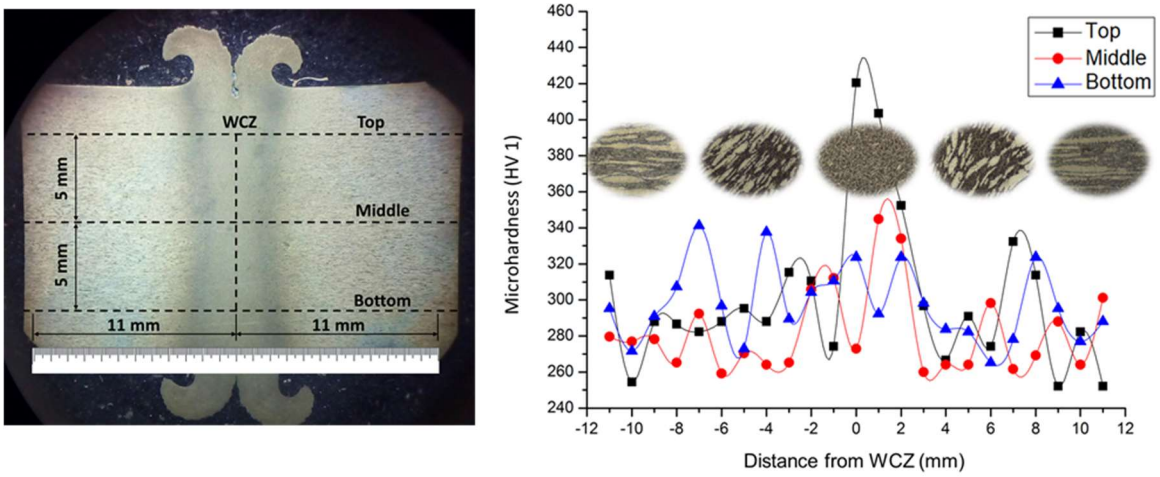

Figure 11. Sample for the HV 1 microhardness test with the scheme adopted for carrying out measurements and results.

4. CONCLUSIONS

Rotary friction welding of the Bronze-Aluminium-Nickel CuAl10Ni5Fe5 alloy proved to be a process capable of performing the solid state joining of this material. Friction time was the most significant factor for heat generation and axial reduction of the workpieces, and, in this sense, the fractional factorial experiment expressed the optimal parameters for friction welding with the rotation of 3000 revolutions per minute, time of friction and forging, respectively, of 15.4 and 15 seconds, friction and forging pressure, in this order, of 0.5 and 5 MPa. Thermography combined with numerical simulation proved to be convenient to indicate the thermal history of the process since there were significant microstructural changes in the welding region, with the emergence of Widmanstätten morphology and Beta (β) phase retained with martensitic structure. The microhardness test indicated an increase in hardness in the weld centre zone, attributing to the material a fragile behavior that was confirmed with the tensile test, in which the mean values of the tensile strength limit, yield strength and total elongation were lower if compared with the material samples before processing the working pieces.

5. ACKNOWLEDGEMENTS

The authors thank the support of the company TERMOMECANICA São Paulo S.A. for the transfer of non-ferrous metallic materials, technical staff and laboratories, the University of ABC for the use of its laboratories and equipment, the ESSS company for granting the Ansys commercial software license and the IFSP - Federal Institute of Education, Science and Technology of São Paulo for the support to carry out this research work.

6. REFERENCES

ABNT NBR ISO 6892-1:2013 - Metallic materials - Tensile testing Part 1: Method of test at room temperature, 2015.
ABNT NBR NM ISO 6507-1:2008 - Metallic materials - Vickers hardness test Part 1: Test method, 2008.
ASTM B249 / B249M-18a. Standard Specification for General Requirements for Wrought Copper and Copper-Alloy Rod, Bar, Shapes and Forgings, ASTM International, West Conshohocken, PA, 2018.
ASTM E3-95, Standard Practice for Preparation of Metallographic Specimens, ASTM International, West Conshohocken, PA, 1995.
ASTM E407-99, Standard Practice for Microetching Metals and Alloys, ASTM International, West Conshohocken, PA, 1999.

Cai, W., Daehn, G., Vivek, A., Li, J., Khan, H., Mishra, R. and Komarasamy, M., 2019. "A State-of-the-Art Review on Solid-State Metal Joining". ASME Journal of Manufacturing Science and Engineering. 141(3):031012-031012-35. doi:10.1115/1.4041182.

Küçükömeroğlu, T. et al. Microstructural and Mechanical Properties of Friction Stir Welded Nickel-Aluminum Bronze (NAB) Alloy. Journal of Materials Engineering and Performance, v. 25, n. 1, p. 320–326, 2016.

Maalekian, M. Friction welding – critical assessment of literature. Science and Technology of Welding and Joining, v. 12, n. 8, p. 738–759, 2007.

Richardson, I., 2016. "Guide to Nickel Aluminum Bronze for Engineers". Copper Development Association publication n. 222.

Schwer, L. Guide for verification and validation in computational solid mechanics. American Society of Mechanical Engineers, v. PTC 60, n. V&V 10, p. 1–15, 2006.

Selvaraju, S. et al. Effect of Process Parameters on Microstructure and Mechanical Properties of Friction Stir Welded Cast Nickel Aluminum Bronze Alloy (C95800). Materials Research, v. 21, n. 3, 2018.

Siva, S. et al. Microstructure and Mechanical Properties of Exothermic-Reaction-Assisted Friction-Stir-Welded Nickel-Aluminum Bronze Alloy. Journal of Materials Engineering and Performance, v. 28, n. 4, p. 2256–2270, 2019.

Thien, N. D., Quang, D.L., Van, T.P. and Anh, T.T., 2016. "A Welding Temperature Determination Method of Low Carbon Steel and Stainless Steel Welded Joint by Rotary Friction Welding Process". 2016 3rd International Conference on Green Technology and Sustainable Development (GTSD), p. 206–211.

Vairis, A.; Papazafeiropoulos, G; Tsainis, A. A comparison between friction stir welding, linear friction welding and rotary friction welding. Advances in Manufacturing. v. 4, n. 4, p. 296-304, 2016.

7. RESPONSIBILITY NOTICE

The authors are the only responsible for the printed material included in this paper.